Excellent Photocatalytic Rhodamine B Degradation for water Remediation Over Pr3+ Doped Bi2WO6 Microspheres

Xianghui Zhang (zxhlynu@163.com)

Henan Key Laboratory of Electromagnetic Transformation and Detection, College of Physics and Electronic Information, Luoyang Normal University, Luoyang, 471934, PR China https://orcid.org/0000-0002-6709-6073

Research Article

Keywords: Pr3+ doing, Photocatalysis, RhB degradation, Hydrothermal method, Microspheres

Posted Date: June 16th, 2021

DOI: https://doi.org/10.21203/rs.3.rs-611760/v1

Excellent photocatalytic rhodamine B degradation for water remediation over Pr^{3+} doped Bi_2WO_6 microspheres

Xianghui Zhang*

Henan Key Laboratory of Electromagnetic Transformation and Detection, College of Physics and Electronic Information, Luoyang Normal University, Luoyang, 471934, PR China

Abstract: In this work, a serious of Pr^{3+} doped Bi_2WO_6 had been prepared by one-step hydrothermal method without using any additive. XRD results showed that the Pr^{3+} doped Bi_2WO_6 possessed pure orthorhombic phase. XRD patterns shifted to higher angles with the doping amount of Pr^{3+} increasing indicated that Pr^{3+} was doped into the lattice of Bi_2WO_6. UV-vis DRS results revealed that the band gap was narrowed by Pr^{3+} doping. SEM and TEM images showed that the Pr^{3+} doped Bi_2WO_6 presented 3D flower-like microspheres constructed by many nanosheets. The photocatalytic activities of the as-prepared samples were evaluated by using rhodamine B (RhB) as the target organic pollutant. It was found that 1% Pr-Bi_2WO_6 exhibited excellent photocatalytic performance, as well as good stability and reusability. The improved photocatalytic activity can be ascribed to the optimum optical absorption activity, the larger specific surface area and the morphology of microspheres which resulted in the effective separation of the photogenerated electron hole pairs. In addition, the photocatalytic mechanism had been discussed according to the radical-trapping experiments.

Keywords: Pr^{3+} doing, Photocatalysis, RhB degradation, Hydrothermal method, Microspheres

* Corresponding author. Tel.: +86 379 68618310. *E-mail address*: zxhlynu@163.com (XH. Zhang)

1. Introduction

With the rapid development of industrialization, large numbers of pollutants have been discharged into the environment irresponsibly. It has caused serious environmental problems worldwide [1,2]. Many methods including physical, chemical, and biologic ones have been taken to solve the environmental problems. However, they all cannot degrade the pollutants completely [3]. Recently, lots of researches have reported that the technology of photodegradation over semiconductors which can generate photogenerated electrons and holes shows great promise for environmental remediation [4]. The electrons and holes can transfer to the semiconductor surface and cause redox reactions in aqueous solution, and thus decomposing pollutions completely to carbon dioxide and water through utilizing solar energy [5].

A lot of excellent semiconductor photocatalysts with high catalytic activity and stability have been prepared so far, such as TiO_2, ZnO, WO_3, $SrTiO_3$, $BiVO_4$, Bi_2WO_6, CdS, $ZnIn_2S_4$, etc. [6-13] Among the various photocatalysts, Bi_2WO_6 has attracted considerable interests because of its excellent physical and chemical properties. Bi_2WO_6 has a band gap of 2.6~2.8 eV that absorbs a reasonable fraction of the solar spectrum, and has high stability, high oxidation power of valence band (VB) holes. Moreover, Bi_2WO_6 is recognized as one of the few n-type semiconductors resistant to photocorrosion in aqueous solutions. Therefore, Bi_2WO_6 has been synthesized in a variety of morphologies, such as microspheres [11,14], nanofibers [15,16], nanosheets [17-19], and nanoflowers [20,21]. However, pure Bi_2WO_6 still has some drawbacks. Its conduction band (CB) edge is relatively low, so it cannot provide sufficient potential to react with electron acceptors strongly, and then directly results in fast recombination and lower photocatalytic activity. Therefore, the development of modified Bi_2WO_6-based photocatalysts is very promising which

can work efficiently under a wide range of light irradiation.

Many studies reveal that doping metallic or nonmetallic element into Bi_2WO_6 can improve its photocatalytic performance. The doping element like Mg, Ni, Ag, Fe, F, N, etc. [22-27] can modify the electronic structure and surface properties of Bi_2WO_6, thus extending its light absorbance. Then, the activity of photocatalyst will be improved. Compared with other metals, rare earth elements are more useful dopants to enhance the photocatalytic performance of Bi_2WO_6 [28-36]. This can be attributed to its ability to form complexes with various Lewis bases (e.g., amines, alcohols, aldehydes, etc.) in the interaction of these functional groups with the f-orbital of the rare earth elements. Thus, incorporation of the rare earth elements can provide an approach to increase the concentration of organic pollutant at the semiconductor surface and therefore enhance the photocatalytic activity of the catalyst.

However, the mentioned papers mostly used surfactant, acid or alkaline agent as additive during the preparation of the rare earth doped Bi_2WO_6 materials, so the application of the materials was limited to some extent. As we all know, there are few reports about the photocatalytic activity of Pr doped Bi_2WO_6. Besides, even if doping the same element into the same material, different results might be obtained by different preparation methods. So, another rare-earth element, Pr, was selected to modify Bi_2WO_6 as a dopant in this work. The Pr doped Bi_2WO_6 was prepared by one-step hydrothermal method without using any additive. The prepared powders were characterized by using X-ray diffraction (XRD), UV-Vis diffuse reflectance spectra (UV-Vis DRS), photoluminescence (PL) spectra, scanning electron microscopy (SEM), transmission electron microscopy (TEM), high-resolution transmission electron microscopy (HRTEM), N_2 adsorption-desorption tests and X-ray photoelectron spectra (XPS). The

65 photocatalytic activities of the as-prepared samples were evaluated by using rhodamine B (RhB)
66 as the target organic pollutant. Results showed that the Pr^{3+} doped Bi_2WO_6 exhibited the highest
67 photocatalytic property, good stability and reusability.

68 **2. Experimental**

69 **2.1. Preparation of photocatalysts**

70 The series of Pr^{3+} doped Bi_2WO_6 photocatalysts were prepared by hydrothermal method. In a
71 typical procedure, 6 mmol of $Bi(NO_3)_3 \cdot 5H_2O$ and a certain amount of $Pr(NO_3)_3 \cdot 6H_2O$ (0, 0.03,
72 0.06, 0.12 or 0.24 mmol) were dissolved in 60 mL of deionized water under stirring at room
73 temperature. Then 3 mmol of $Na_2WO_4 \cdot 2H_2O$ joined in the above solution to stir for 10 min. After
74 that, the mixture was transferred into the high-pressure reaction kettle and maintained at 160 °C
75 for 24 h. Afterwards the precipitate was repeatedly filtered and washed with deionized water for
76 several times when the reaction kettle was naturally cooled to room temperature. Finally, the
77 powder products were obtained after dried at 80 °C for 8 h, and labeled as Bi_2WO_6, 0.5%
78 Pr-Bi_2WO_6, 1% Pr-Bi_2WO_6, 2% Pr-Bi_2WO_6 and 4% Pr-Bi_2WO_6, respectively.

79 **2.2. Characterization**

80 X-ray diffractometer (D8 Advance, Bruker) determined the crystalline phases of the samples
81 in a wide angle range (2θ = 20 – 80°). UV-Vis-near-IR spectrophotometer (UV-3600 plus,
82 Shimadzu) measured the diffuse reflectance spectra of the samples in the 250 – 800 nm range at
83 room temperature using $BaSO_4$ as a reference. Fluorescence spectrophotometer (F-7000, Hitachi)
84 recorded the photoluminescence spectra. Field-emission scanning electron microscope (Sigma 500,
85 ZEISS), transmission electron microscopy, and high-resolution transmission electron microscopy
86 (JEM-2100F, JEOL) observed the typical morphologies and microstructures. X-ray photoelectron

spectrometer (EscaLab 250Xi, Thermo Fisher) collected the X-ray photoelectron spectra using an Al Kα source. Specific surface and porosity analyzer (ASAP 2020 Plus HD88, Micromeritics) measured the N_2 adsorption-desorption isotherms at liquid nitrogen temperature. The pore size distribution was obtained from the N_2-desorption branch by the Barrett-Joyner-Halenda (BJH) method.

2.3. Photocatalytic reactions

The photocatalytic performance of the samples was estimated by photocatalytic degradation of the RhB. A 300 W Xe lamp was used as the light source in the photoreaction system. Typically, 0.1 g of the photocatalyst was dispersed in 100 mL of the RhB aqueous solution with an initial concentration of 10^{-5} mol·L^{-1} in a quartz reactor, which was exposed to air to ensure sufficient oxygen supply for the reaction. Before irradiation, the suspension was magnetically stirred in dark for 30 min to ensure the establishment of an adsorption/desorption equilibrium. Then, the suspension was exposed to irradiation under magnetic stirring. The temperature of the suspension was maintained at about 35 °C during the photodegradation reaction process. At 10 min interval, an aliquot of 3 mL of the suspension was taken and then centrifuged to remove the particles. The optical absorption spectra for the supernatant solution were recorded by a Shimadzu UV-3600 plus UV-vis-near-IR spectrophotometer. The photodegradation efficiency η was calculated according to the formula (1)

$$\eta = (c_0 - c)/c \quad (1)$$

where c is the concentration of the RhB pollutant after reaction at time t, and c_0 is the initial concentration when adsorption/desorption equilibrium was achieved.

The remainder of the RhB solution was centrifuged and washed thoroughly with deionized

water after the above photocatalytic degradation experiments to study the stability and reusability of the photocatalyst. Then, the photocatalyst was dried at 60 °C in air for 12 h and reused in the next cycle.

The radical-trapping experiments were performed to investigate the mechanism of photocatalytic degradation. In order to determine the main active species in the photocatalytic reaction, various scavengers were added into the RhB solution. Ethylenediaminetetraacetic acid disodium salt (EDTA-2Na, mmol·L^{-1}), p-Benzoquinone (p-BQ, 5 mmol·L^{-1}) and isopropanol (IPA, mmol·L^{-1}) were used as a scavenger for photogenerated hole (h^+), superoxide radical ($\cdot O^{2-}$), hydroxyl radical (·OH), respectively. The next experimental processes were similar to the above photocatalytic test.

3. Results and discussion

3.1. Crystal structure

Figure 1a depicted the crystal structure and phase purity investigated by XRD for the as-prepared samples. From the figure, it can be seen that the distinct diffraction peaks appearing at about 28.30°, 32.79°, 47.15°, 55.82°, 58.54°, 68.73°, 76.07°and 78.49° are indexed to an orthorhombic phase Bi_2WO_6 (PDF Card No. 79-2381) [17]. The XRD patterns for all the as-prepared samples are very similar, indicating that the Pr^{3+} doing do not change the crystal structure of Bi_2WO_6. There are no characteristic peaks related to impurity phases, confirming that the samples are pure. The sharp and intense diffraction peaks indicate the crystalline nature of the as-prepared samples. Furthermore, the peaks are progressively become weak and broad from Bi_2WO_6 to 4% Pr-Bi_2WO_6 with increasing Pr^{3+} doping amount, implying that Pr^{3+} successfully incorporated into B_2WO_6 and inhibit the grain growth of Bi_2WO_6 [22,34]. The average size of the

as-prepared samples was estimated based on the strongest peak at about 28.30° according to the Scherrer formula. The result shows that the average crystallite size is about 16.1, 12.3, 13.0, 11.4, and 11.4 nm for Bi_2WO_6, 0.5% Pr-Bi_2WO_6, 1% Pr-Bi_2WO_6, 2% Pr-Bi_2WO_6 and 4% Pr-Bi_2WO_6, respectively. It clearly shows that the crystallite size decreased significantly when Pr^{3+} doping into Bi_2WO_6. The reason for the decrease maybe that the defects will appear on the surface of the photocatalyst after Pr^{3+} doping, which can inhibit the growth of the crystal [36]. The small crystallite size means a short migration distance and a low recombination rate of the photogenerated electron-hole pairs, so the photocatalytic activity may become better. It was also noted that the diffraction peaks were slightly shifted to higher angles with the amount of Pr^{3+} doped increasing, as shown in Figure 1b. These results clearly indicated that Pr^{3+} was incorporated into the lattice of B_2WO_6, because the ionic radius of Pr^{3+} (0.99 Å) is smaller than the radius of Bi^{3+} (1.03 Å) [35].

3.2. UV-Vis diffused reflection spectra

Figure 2a shows the UV-Vis diffused reflection spectra of the as-prepared samples. It can be observed from the figure that there is a strong absorption edge in the region below 450 nm for each sample. This indicates that the light absorption of the sample is caused by the transition of energy band structure, rather than the transition of impurity level [23]. At the same time, the absorption edge of the series of samples first moves slightly to the long wave edge, and then to the short wave edge. In addition, It can also be observed that Pr^{3+} doped Bi_2WO_6 samples have higher light absorption than undoped Bi_2WO_6 sample in the visible region of larger than 450 nm. These indicate that the doping of Pr^{3+} in Bi_2WO_6 can extend the light absorption region and improve the optical absorption efficiency of the samples. The enhanced light absorption may be ascribed to the

charge transfer between Bi_2WO_6 valence band or conduction band and Pr 3d orbit, as well as the lattice defects caused by Pr^{3+} doping.

The band gap energy (E_g) of the above samples was estimated using Tauc formula:

$$\alpha h\nu = A(h\nu - E_g)^{n/2} \quad (2)$$

where α is the absorption coefficient, h is Planck's constant, ν is the photon's frequency, A is a proportional constant. The value of the exponent n denotes the nature of the sample transition. For direct allowed transition n = 1 and for indirect allowed transition n = 4 [25,37]. Bi_2WO_6 is an indirect allowed transition semiconductor, so the value of n is 4. By linear fitting of the curve, the intersection point of the fitted line and the horizontal axis is the band gap energy of the samples. According to the $(\alpha h\nu)^{0.5}$-$h\nu$ curve (Figure 2b), the band gap energy values are 2.54 eV, 2.53 eV, 2.48 eV, 2.49 eV and 2.51 eV for B_2WO_6, 0.5% Pr-B_2WO_6, 1% Pr-B_2WO_6, 2% Pr-B_2WO_6 and 4% Pr-B_2WO_6, respectively. It can be seen that, compared with B_2WO_6, the band gap energy of the Pr^{3+} doped B_2WO_6 samples becomes narrow. The changes of band gap energy may be attributed to the formation of an impurity level due to the incorporation of Pr. A narrower band gap means enhanced light absorbing properties, and it is helpful for electron excitation from the valence band to the conduction band. Hence, the 1% Pr-B_2WO_6 sample may have enhanced photocatalytic activity. However, the band gap energy became larger with excessive Pr^{3+} ion doping. The reason for the change in band gap energy may be the Pr 3d orbital will be hybridized with the conduction band bottom (W 5d orbital) of Bi_2WO_6 to form a hybrid energy level instead of forming a new doping level in the forbidden band of Bi_2WO_6 when the doping amount is excessive. This is a common phenomenon of metal-doped B_2WO_6 materials [24,36]. The variation trend of the band gap energy value is also consistent with the UV-Vis diffuse reflectance spectra of the samples

shown in Figure 2a.

3.3. Photoluminescence spectra

Since photoluminescence (PL) is mainly derived from the recombination of photogenerated carriers in semiconductors, the PL spectrum is often used to characterize the recombination rate of carriers. Generally, the higher the photoluminescence spectral intensity is, the higher the photogenerated electrons and holes recombination rate is. Figure 3 shows the photoluminescence spectra of undoped Bi_2WO_6 and 1% Pr-Bi_2WO_6. The recombination rate of photogenerated electrons and holes is the main factor affecting the photocatalytic activity. The smaller the intensity of photoluminescence spectrum means the smaller the recombination rate of the electron-hole pairs and the higher photocatalytic activity. Compared with the undoped Bi_2WO_6 sample, the position of the photoluminescence characteristic peak for the doped sample is almost unchanged, but the intensity of the photoluminescence spectrum is weaker, which is consistent with its better photocatalytic performance. The result indicates that the doping of Pr^{3+} improves the separation efficiency of photogenerated electrons and holes, effectively reducing the recombination rate of the electron-hole pairs, and promoting its photocatalytic activity.

3.4. X-ray photoelectron spectra

The surface chemical composition and chemical valence of the related elements in Bi_2WO_6 and 1% Pr-Bi_2WO_6 sample were analyzed by X-ray photoelectron spectroscopy (XPS). As can be seen from the survey spectra (Figure 4a), the samples mainly contain elements of Bi, W, O and C, of which C comes from the instrument and the environment. These elements of B, W and O are consistent with their chemical compositions. The high-resolution XPS spectra of Bi 4f, W 4f, O 1s and Pr 3d are shown in Figure 4b-e. In Figure 4b, the XPS signal peaks located at 159.1 eV and

164.4 eV correspond to $4f_{7/2}$ and $4f_{5/2}$ of Bi^{3+}, respectively [38]. Figure 4c shows that the binding energies of W $4f_{7/2}$ and W $4f_{5/2}$ are respectively 35.4 eV and 37.5 eV, indicating that W element exists in the form of W^{6+} [39]. In figure 4d, the asymmetric signal peak of O 1s is divided into three peaks: 529.9 eV, 530.8 eV, and 532.1 eV, which are attributed to the lattice oxygen, hydroxyl groups, and physisorbed water, respectively [40]. From Figure 4e, it is found that the Pr 3d spectrum can be fully described by the two sets of spin-orbital multiplets, corresponding to the $3d_{3/2}$ and $3d_{5/2}$ contributions and two peaks for each contribution. The peaks labeled m (954.3 eV) and s (947.6 eV) are assigned to $3d_{3/2}$ of Pr^{3+}, and the peaks denoted as m' (933.2 eV) and s' (929.1 eV) correspond to $3d_{5/2}$ of Pr^{3+} [41]. Furthermore, the real molar ratio of Bi, W and O atoms from the XPS result was about 1.95 : 1 : 6.26, which was close to the theoretical value. However, the real percentage of the Pr^{3+} content doped into Bi_2WO_6 was about 0.7%, which was a little less than the theoretical amount of the dopant in the experiment (1%).

3.5. Morphology

The morphology of the undoped Bi_2WO_6 and 1% Pr-Bi_2WO_6 samples is shown in Figure 5. It can be clearly observed from the figure that the morphologies of the two samples are similar, which are assembled into 3D flower-like microspheres structure with a diameter of about 2-3 μm from a large number of 2D lamellar structure. The lamellar structure is further composed of many nanometer squares with a length of about 200 nm. The flower-like microspheres structure greatly increases the specific surface area of the samples, further increases the contact area between the samples and the pollutant, and promotes the reaction with the pollutant, thus shortening the degradation time and improving the degradation efficiency. At the same time, the lamellar structure is interwoven to form an open porous structure. These pores of different diameters may

219 change the physical and chemical properties of the samples and become transport channels for
220 small molecules, which is conducive to the full reaction of photocatalyst and pollutant. After Pr^{3+}
221 doping, the morphology of flower-like microspheres is less regular and becomes more loosely,
222 leading to the improvement of specific surface area. Therefore, the morphology change of the
223 doped Bi_2WO_6 sample is beneficial to improve its photocatalytic activity.

224 Figure 6 shows the TEM and HRTEM images of 1% Pr-Bi_2WO_6 sample. It can be clearly
225 observed that the sample demonstrates microspheres structure with diameter of about 2-3 μm
226 (Figure 6a). The microspheres are constructed by many nanoscale squares, and the squares with
227 edge length ranging from 100 to 200 nm stacked face-to-face (Figure 6b). The results are
228 consistent with the SEM analysis. The HRTEM images (Figure 6c, d) reveal that its lattice fringe
229 is 0.32 nm, which are corresponding to (131) crystallographic planes of Bi_2WO_6. As XPS results
230 showed, the actual Pr^{3+} content is very low, so the correlative lattice fringes of Pr^{3+} oxide cannot
231 be observed in HRTEM image.

232 **3.6. Physisorption Property**

233 The physisorption properties of the as-prepared samples were estimated using the N_2 gas
234 adsorption-desorption data. Figure 7 shows the N_2 gas adsorption-desorption isotherms of the
235 undoped Bi_2WO_6 and 1% Pr-Bi_2WO_6 samples (Figure 7a and 7b) and the pore size distribution
236 curves (Figure 7c and 7d). It can be seen from the figure that both isotherms of the two samples
237 are very similar, which belong to the type II curve according to the IUPAC classification, implying
238 the possible existence of slit-like pores [42]. The shape of the hysteresis loops displays a H3 loop,
239 suggesting the samples are loose accumulation with lamellar particles [43]. In figure 7c, the
240 undoped Bi_2WO_6 sample exhibits a wide pore size distribution of 3.7-75 nm, confirming the

241 presence of mesopores and macropores. But in figure 7d, the 1% Pr-Bi_2WO_6 sample shows its
242 maximum pore size distribution in the region of 3.8 nm and pore size distribution in the region of
243 3-50 nm, indicating the existence of slit-like pores and mesopores. The specific surface areas of
244 the undoped Bi_2WO_6 and 1% Pr-Bi_2WO_6 samples were 12.27 and 20.10 $cm^2 \cdot g^{-1}$. It can be seen
245 that the specific surface area of the 1% Pr-Bi_2WO_6 sample is more than 60% higher than that of
246 the undoped Bi_2WO_6 sample. This indicates that after Pr^{3+} doping, the crystal growth of Bi_2WO_6
247 is inhibited, thus increasing the specific surface area, so the 1% Pr-Bi_2WO_6 sample may have
248 better performance in photocatalysis.

249 **3.7. Photocatalytic properties**

250 The adsorption capability and the photocatalytic activity of the as-prepared samples were
251 estimated by the adsorption and the degradation of RhB dye, respectively.

252 The adsorption curves of RhB in the presence of the as-prepared samples are shown in Figure
253 8. The curves exhibit that the adsorption of RhB is very fast in the initial 5 min, then gradually
254 slowed down, and reached equilibrium within 30 min. The 1% Pr-Bi_2WO_6 sample exhibited the
255 best adsorption capability among the studied samples. The phenomenon may indicate that the 1%
256 Pr-Bi_2WO_6 sample have the largest surface area, because larger surface area means more active
257 sites that are beneficial for the adsorptionof the RhB dye.

258 The photocatalytic properties of Pr^{3+} doped Bi_2WO_6 samples were evaluated by the
259 degradation efficiency of RhB. Figure 9 shows the UV-Vis spectra of RhB at different
260 photocatalytic degradation times catalyzed by the 1% Sm-Bi_2WO_6 sample. The absorption peak at
261 about 554 nm is the characteristic absorption peak of RhB, which corresponds to the large
262 conjugate system composed of benzene ring, double bond and heterocycle in RhB molecule. The

263 characteristic peak decreases sharply after the light is turned on, indicating that RhB molecules
264 were quickly decomposed [32,44]. After 20 min of illumination, the absorption peak almost
265 coincides with the baseline, that is, RhB are well degraded, indicating that the aromatic ring
266 structure of dye molecules is destroyed and deethylation is carried out simultaneously. The color
267 of the RhB solution also changes from pink to pale yellow and then, the solution becomes
268 colorless. This suggests the complete decolorization of the RhB solution

269 Figure 10a shows the effect of Pr^{3+} doping on RhB degradation. As is shown in the figure,
270 RhB has good stability under irradiation when there is no photocatalyst, indicating that the
271 self-sensitized degradation of RhB does not occur. When the photocatalyst is added into the
272 reaction solution, the undoped and Pr^{3+} doped Bi_2WO_6 all have good removal effect on RhB under
273 the same condition, and the removal amount of RhB increases as the Pr^{3+} doping amount increases
274 from 0.005% to 0.01%. But it decreases with the doping amount continued to increase. The
275 photocatalytic degradation rate of RhB is only 74.2% after 20 min of illumination when the
276 undoped Bi_2WO_6 sample is used as photocatalyst, and it can reach 99.4% when the photocatalyst
277 is replaced by 1% Pr-Bi_2WO_6 sample. The RhB concentration and photodegradation time were
278 linearly regressed using the first-order rate equation to obtain the reaction rate constant of the
279 photocatalytic system under different conditions, and the results are shown in figure 10b. As is
280 shown in figure 10b, the reaction rate constant of the 1% Pr-Bi_2WO_6 sample (0.25752 min^{-1})
281 obviously becomes much larger, which is about 3.9 times of that of the undoped Bi_2WO_6 sample
282 (0.06673 min^{-1}). In contrast, the reaction rate constant of the 2% Pr-Bi_2WO_6 and 4% Pr-Bi_2WO_6
283 samples downs to 0.05965 and 0.02823 min^{-1}, respectively. Therefore, the results show that the
284 appropriate doping amount can greatly improve the photodegradation activity of RhB, while an

285 excessive doping amount is unfavorable for photodegradation. Moreover, the photocatalytic
286 performance of 1% Pr-Bi_2WO_6 sample prepared in this paper was compared with other rare earth
287 doped Bi_2WO_6 samples based on previous reports (Table 1). It is observed that the photocatalyst
288 prepared in this paper shows much higher degradation efficiency than those in references.
289 Therefore, the 1% Pr-Bi_2WO_6 sample has rather excellent photocatalytic performance.

290 The reason why the photocatalyst doped by rare earth element can improve its photocatalytic
291 activity is pointed out by Li et al. [45], which may be mainly due to the quantum effect and
292 specific structural characteristics (such as the improvement of specific surface area and the
293 reduction in crystallite size), while El-Bahy et al. [46] considered that the photocatalytic materials
294 have stronger adsorption capacity and light absorption capacity after doping rare earth elements.
295 According to the previous characterization, a certain amount of Pr replaces Bi in Bi_2WO_6, more
296 photogenerated carriers are produced due to the decreased band gap energy, and the recombination
297 rate of photogenerated electrons and holes is reduced because of the forming of lattice defects. In
298 addition, after Pr^{3+} doping, the contact area between photocatalyst and pollutant increases with the
299 specific surface area of the sample increases, the migration distance of photogenerated carriers
300 decreases with the crystallite size of the sample decreases. Therefore, the photocatalytic
301 performance of the sample was improved by speeding up the migration rate of photogenerated
302 carriers and reducing the recombination rate of photogenerated electrons and holes. When the
303 doping amount is 1%, the sample has the best photocatalytic activity due to its optimal specific
304 surface area and electron-hole recombination rate. However, when excess amount of Pr^{3+} doped
305 into Bi_2WO_6, the dopant may cover the active sites on the surface of Bi_2WO_6, thus, the
306 photogenerated electrons and holes cannot be transferred effectively, leading to the reduction in

307 photocatalytic activity.

308 Figure 11 shows the photocatalytic degradation of RhB over 1% Pr-Bi_2WO_6 during four
309 catalytic cycles. It can be seen that the photocatalyst still retains strong photocatalytic activity
310 after repeated use for 4 times. The photodegradation efficiency was still about 95% at the fourth
311 cycle. This implies that the as-prepared photocatalyst is a good photocatalyst with high activity,
312 stability, and reusability. However, the effect was not as good as that of the first application, which
313 may be because some products were still adsorbed on the surface of the photocatalyst after the
314 first cycle, which affected the subsequent experiments. In addition, due to incomplete transfer, part
315 of the photocatalyst was lost in the process of reuse.

316 In order to study the photocatalytic mechanism of RhB photodegradation, various scavengers
317 were added during the photocatalytic process to explore the main active species in the
318 photodegradation reaction, the results are shown in Figure 12. In this study, EDTA-2Na, p-BQ and
319 IPA were added as scavenger for h^+, $\cdot O^{2-}$ and $\cdot OH$, respectively. As can be seen from the figure,
320 the photodegradation efficiency of RhB is 99.4% when no scavenger is added. Under the same
321 conditions, the efficiency is reduced to 96.9%, 93.5% and 2.2% after p-BQ, IPA and EDTA-2Na
322 were added, respectively. This indicates that h^+ is the main active species in the photocatalytic
323 system, while$\cdot O^{2-}$ and $\cdot OH$ have little effect on photodegradation of RhB.

324 Based on the UV-Vis diffused reflection spectra results, the conduction band edge (CB) and
325 valance band edge (VB) positions of of the as-prepared samples are estimated by mulliken
326 electronegativity model [37,47]:

327 $$E_{CB} = X - E_e - 0.5E_g \quad (3)$$

328 $$E_{VB} = E_{CB} + E_g \quad (4)$$

where X is the electronegativity of semiconductor and E_e is the energy of free electrons on the hydrogen scale (about 4.5 eV). The X value for Bi_2WO_6 is 6.38 eV [37]. According to above equations, the VB of Bi_2WO_6 and 1% Pr- Bi_2WO_6 was estimated to be 3.12 eV and 3.09 eV, respectively. As a result, the CB positions were also determined to be 0.58 eV and 0.61 eV, respectively. Figure 13 displays the diagram of the energy band levels of 1% Pr-Bi_2WO_6 and the proposed possible process for the photodegradation of RhB. Due to the intrinsic physical and chemical properties of Bi_2WO_6, the photogenerated electrons (e^-) in CB can be easily excited under light irradiation, and the holes (h^+) existed in VB. The band gap decreased after doped with Pr^{3+} ions, which favored the electron transition from VB to CB (Eq. 5). A majority of h^+ in VB of 1% Pr-Bi_2WO_6 can be mostly used for the direct oxidation of RhB (Eq. 6), and the other part of h^+ can be captured by H_2O to form ·OH (Eq. 7), because the potential of the holes at the VB of 1% Pr-Bi_2WO_6 (3.09 eV) is more positive than the redox potential of ·OH/H_2O (2.68 eV). The resulting ·OH can also decompose a small amount of RhB (Eq. 8). The e^- in CB of 1% Pr-Bi_2WO_6 cannot directly reduce O_2 to $\cdot O_2^-$, because the CB of 1% Pr-Bi_2WO_6 (0.61 eV) is not negative enough compared to the reduction potential of $O_2/\cdot O_2^-$ (0.13 eV). The probable reactions can be summarized by the following equations:

$$1\%\ \text{Pr-}Bi_2WO_6 + h\nu \rightarrow 1\%\ \text{Pr-}Bi_2WO_6\ (h^+ + e^-) \quad (5)$$

$$h^+ + \text{RhB} \rightarrow \text{degraded products} \quad (6)$$

$$h^+ + H_2O \rightarrow \cdot OH \quad (7)$$

$$\cdot OH + \text{RhB} \rightarrow \text{degraded products} \quad (8)$$

4. Conclusions

A series of flower-like Pr^{3+} doped Bi_2WO_6 microspheres were prepared by one-step

hydrothermal method. After Pr^{3+} doping, the photocatalytic performance of Bi_2WO_6 was significantly improved. When the doping amount of Pr^{3+} is 1%, the photocatalytic degradation performance of the sample was the best. After 20 min of irradiation, the degradation efficiency of RhB reaches 99.4%, which is increased by 25% compared with that of Bi_2WO_6 without doping. Doped Pr^{3+} can improve the specific surface area and reduce the recombination rate of photogenerated electrons and holes of the sample, thus improving the photocatalytic performance of the sample.

Declarations

Funding: The study was funded by the Henan Provincial Department of Science and Technology Research Project (No. 182102311047).

Conflicts of interest/Competing interests: The authors declare that they have no conflict of interest or competing interests.

Availability of data and material: All data generated or analyzed during this study are included in this published article.

Code availability: Not applicable

References

[1] F. Chen, Z. Ma, L. Ye, T. Ma, T. Zhang, Y. Zhang, H. Huang, Macroscopic spontaneous polarization and surface oxygen vacancies collaboratively boosting CO_2 photoreduction on $BiOIO_3$ single crystals. Adv. Mater. **32**, 1908350 (2020) https://doi.org/10.1002/adma.201908350

373 [2] S. Wang, X. Han, Y. Zhang, N. Tian, T. Ma, H. Huang, Inside-and-out semiconductor
374 engineering for CO_2 photoreduction: From recent advances to new trends. Small Structures **2**,
375 2000061 (2020) https://doi.org/10.1002/sstr.202000061
376 [3] Z. Pei, H. Jia, Y. Zhang, P. Wang, Y. Liu, W. Cui, J. Xu, J. Xie, A One-pot hydrothermal
377 synthesis of Eu/$BiVO_4$ enhanced visible-light-driven photocatalyst for degradation of
378 tetracycline. J. Nanosci. Nanotechno. **20**, 3053–3059 (2020)
379 https://doi:10.1166/jnn.2020.17446
380 [4] S. Asadzadeh-Khaneghah, A. Habibi-Yangjeh, g-C_3N_4/carbon dot-based nanocomposites serve
381 as efficacious photocatalysts for environmental purification and energy generation: A review.
382 J. Clean. Prod. **276**, 124319 (2020) https://doi.org/10.1016/j.jclepro.2020.124319
383 [5] X. Li, J. Xiong, X. Gao, J. Ma, Z. Chen, B. Kang, J. Liu, H. Li, Z. Feng, J. Huang, Novel
384 BP/BiOBr S-scheme nano-heterojunction for enhanced visible-light photocatalytic
385 tetracycline removal and oxygen evolution activity. J. Hazad. Mater. **387**, 121690 (2019)
386 https://doi:10.1016/j.jhazmat.2019.121690
387 [6] D. Huang, H. Liu, J. Bian, T. Li, B. Huang, Q. Niu, High specific surface area TiO_2
388 nanospheres for hydrogen production and photocatalytic activity. J. Nanosci. Nanotechno. **20**,
389 3217–3224 (2020) https://doi:10.1166/jnn.2020.17380
390 [7] M. Golmohammadi, M. Honarmand, S. Ghanbari, A green approach to synthesis of ZnO
391 nanoparticles using jujube fruit extract and their application in photocatalytic degradation of
392 organic dyes. Spectrochim. Acta A **229**, 17961 (2020) https://doi:10.1016/j.saa.2019.117961
393 [8] G. Zheng, J. Wang, H. Liu, V. Murugadoss, G. Zu, H. Che, C. Lai, H. Li, T. Ding, Q. Gao, Z.
394 Guo, Tungsten oxide nanostructures and nanocomposites for photoelectrochemical water

splitting. Nanoscale **11**, 18968–18994 (2019) https://doi:10.1039/C9NR03474A

[9] P.L. Hsieh, G. Naresh, Y.S. Huang, C.W. Tsao, Y.J. Hsu, L.J. Chen, M.H. Huang, Shape-tunable $SrTiO_3$ crystals revealing facet-dependent optical and photocatalytic properties. J. Phys. Chem. C **123**, 13664–13671 (2019) https://doi:10.1021/acs.jpcc.9b02081

[10] X. Tian, Y. Zhu, W. Zhang, Z. Zhang, R. Hua, Preparation and photocatalytic properties of Mo-doped $BiVO_4$. J. Mater. Sci.: Mater. Electron. **30**, 19335–19342 (2019) https://doi:10.1007/s10854-019-02295-9

[11] X. Zhang, W. Gai, Effect of surfactant on the photocatalytic activity of Bi_2WO_6 nanoparticles. J. Mater. Sci.: Mater. Electron. **28**, 9777–9781 (2017) https://doi:10.1007/s10854-017-6730-z

[12] X. Ning, G. Lu, Photocorrosion inhibition of CdS-based catalysts for photocatalytic overall water splitting. Nanoscale **12**, 1213–1223 (2020) https://doi:10.1039/C9NR09183A

[13] C. Cheng, D. Chen, N. Li, Q. Xu, H. Li, J. He, J. Lu, $ZnIn_2S_4$ grown on nitrogen-doped hollow carbon spheres: An advanced catalyst for Cr(VI) reduction. J. Hazard. Mater. **391**, 122205 (2020) https://doi:10.1016/j.jhazmat.2020.122205

[14] M. Chen, Y. Huang, S. Lee, Salt-assisted synthesis of hollow Bi_2WO_6 microspheres with superior photocatalytic activity for NO removal. Chin. J. Catal. **38**, 348 (2017) https://doi:10.1016/S1872-2067 (16)62584-6

[15] A. Yang, Y. Han, S. Li, H. Xing, Y. Pan, W. Liu, Synthesis and comparison of photocatalytic properties for Bi_2WO_6 nanofibers and hierarchical microspheres. J. Alloy. Comp. **695**, 915–921 (2017) https://doi:10.1016/j.jallcom.2016.10.188

[16] G. Li, Electrospinning fabrication and photocatalytic activity of Bi_2WO_6 nanofibers. J. Mater. Sci.: Mater. Electron. **28**, 12320–12325 (2017) https://doi:10.1007/s10854-017-7050-z

417 [17] X. Hu, J. Tian, Y. Xue, Y. Li, H. Cui, Bi_2WO_6 Nanosheets decorated with Au nanorods for
418 enhanced near-Infrared photocatalytic properties based on surface plasmon resonance effects
419 and wide-range near-infrared light harvesting. ChemCatChem **9**, 1511–1516 (2017)
420 https://doi:10.1002/cctc.201601719
421 [18] G. Zhang, J. Cao, G. Huang, J. Li, D. Li, W. Yao, T. Zeng, Facile fabrication of well-polarized
422 Bi_2WO_6 nanosheets with enhanced visible-light photocatalytic activity. Catal. Sci. Technol. **8**,
423 6420–6428 (2018) https://doi:10.1039/C8CY01963K
424 [19] S. Hu, B. Wang, Y. Ma, M. Li, L. Zhang, Z. Huang, Ultrathin bismuth tungstate nanosheets as
425 an effective photo-assisted support for electrocatalytic methanol oxidation. J. Colloid. Interf.
426 Sci. **552**, 179–185 (2019) https://doi:10.1016/j.jcis.2019.05.048
427 [20] S. Luo, J. Ke, M. Yuan, Q. Zhang, P. Xie, L. Deng, S. Wang, $CuInS_2$ quantum dots embedded
428 in Bi_2WO_6 nanoflowers for enhanced visible light photocatalytic removal of contaminants.
429 Appl. Catal. B **221**, 215–222 (2018) https://doi:10.1016/j.apcatb.2017.09.028
430 [21] Y. Zhao, Y. Wang, E. Liu, J. Fan, X. Hu, Bi_2WO_6 nanoflowers: An efficient visible light
431 photocatalytic activity for ceftriaxone sodium degradation. Appl. Surf. Sci. **436**, 854–864
432 (2018) https://doi:10.1016/j.apsusc.2017.12.064
433 [22] Y. Wang, J. He, D. Peng, T. Zhang, F. Long, X. Zhang, Enhanced photocatalytic performance
434 of Mg^{2+} doped Bi_2WO_6 under simulated visible light irradiation. Ionics **24**, 2893–2903 (2018)
435 https://doi:10.1007/s11581-017-2394-1
436 [23] L. Xiang, L. Chen, C. Mo, L. Zheng, Z. Yu, Y. Li, Q. Cai, H. Li, W. Yang, D. Zhou, M. Wong,
437 Facile synthesis of Ni-doping Bi_2WO_6 nano-sheets with enhanced adsorptive and visible-light
438 photocatalytic performances. J. Mater. Sci. **53**, 7657–7671 (2018)

439 https://doi:10.1007/s10853-018-2064-3

440 [24] N.D. Phu, L.H. Hoang, P.V. Hai, T.Q. Huy, X. Chen, W.C. Chou, Photocatalytic activity
441 enhancement of Bi_2WO_6 nanoparticles by Ag doping and Ag nanoparticles modification. J.
442 Alloy. Comp. **824**, 153914 (2020) https://doi:10.1016/j.jallcom.2020.153914

443 [25] T. Hu, H. Li, N. Du, W. Hou, Iron-doped bismuth tungstate with an excellent photocatalytic
444 performance. ChemCatChem **10**, 3040–3048 (2018) https://doi:10.1002/cctc.201701965

445 [26] H. Yu, C. Chu, X. An, Enhanced visible-light-driven photocatalytic activity of F doped
446 reduced graphene oxide- Bi_2WO_6 photocatalyst: Enhanced photocatalytic activity of F-doped
447 rGO-BWO photocatalyst. Appl. Organomet. Chem. **33**, 4682 (2019)
448 https://doi:10.1002/aoc.4682

449 [27] L. Hoang, N. Phu, H. Peng, X. Chen, High photocatalytic activity N-doped Bi_2WO_6
450 nanoparticles using a two-step microwave-assisted and hydrothermal synthesis. J. Alloy.
451 Comp. **744**, 228–233 (2018) https://doi:10.1016/j.jallcom.2018.02.094

452 [28] F. Zhang, R. Sun, R. Li, N. Song, L. Feng, S. Zhong, Z. Zhao, Novel La-doped Bi_2WO_6
453 photocatalysts with enhanced visible-light photocatalytic activity. J. Sol-gel Sci. Techn. **86**,
454 640–649 (2018) https://doi:0.1007/s10971-018-4683-1

455 [29] J. Li, G. Ni, Y. Han, Y. Ma, Synthesis of La doped Bi_2WO_6 nanosheets with high visible light
456 photocatalytic activity. J. Mater. Sci.: Mater. Electron. **28**, 10148–10157 (2017)
457 https://doi:10.1007/s10854-017-6777-x

458 [30] H. Gu, L. Yu, J. Wang, M. Ni, T. Liu, F. Chen, Tunable luminescence and enhanced
459 photocatalytic activity for Eu(III) doped Bi_2WO_6 nanoparticles. Spectrochim. Acta Part A **177**,
460 58–62 (2017) https://doi:10.1016/j.saa.2017.01.034

461 [31] L. Hoang, N. Phu, P. Chung, P. Guo, X. Chen, W. Chou, Photocatalytic activity enhancement
462 of Bi_2WO_6 nanoparticles by Gd-doping via microwave assisted method. J. Mater. Sci.: Mater.
463 Electron. **28**, 12191–12196 (2017) https://doi:10.1007/s10854-017-7034-z
464 [32] H.A. Ahsaine, M. Ezahri, A. Benlhachemi, B. Bakiz, S. Villain, F. Guinneton, J. Gavarri,
465 Novel Lu-doped Bi_2WO_6 nanosheets: Synthesis, growth mechanisms and enhanced
466 photocatalytic activity under UV-light irradiation. Ceram. Int. **42**, 8552–8558 (2016)
467 https://doi:10.1016/j.ceramint.2016.02.082
468 [33] Z. Liu, X. Liu, L. Wei, C. Yu, J. Yi, H. Ji, Regulate the crystal and optoelectronic properties
469 of Bi_2WO_6 nanosheet crystals by Sm^{3+} doping for superior visible-light-driven photocatalytic
470 performance. Appl. Surf. Sci. **508**, 145309 (2020) https://doi:10.1016/j.apsusc.2020.145309
471 [34] H. Li, W. Li, X. Liu, C. Ren, X. Miao, X. Li, Engineering of Gd/Er/Lu-triple-doped Bi_2MoO_6
472 to synergistically boost the photocatalytic performance in three different aspects:
473 Oxidizability, light absorption and charge separation. Appl. Surf. Sci. **463**, 556 – 565 (2019)
474 https://doi:10.1016/j.apsusc.2018.08.254
475 [35] X. Zhang, M. Wang, X. Jia, K. Cao, M. Zhang, Synthesis and enhanced photocatalytic
476 activity of rare earth ion Ce^{3+}, Nd^{3+}, Pr^{3+} or Sm^{3+}) doped Bi_2WO_6 microspheres for
477 rhodamine B degradation. ChemistrySelect **4**, 12785–12793 (2019)
478 https://doi:10.1002/slct.201903621
479 [36] X. Zhang, M. Zhang, K. Cao, Hydrothermal synthesis of Sm-doped Bi_2WO_6 flower-like
480 microspheres for photocatalytic degradation of rhodamine B. CrystEngComm **21**, 6208–6218
481 (2019) https://doi:10.1039/C9CE01043B
482 [37] N. Tahmasebi, Z. Maleki, P. Farahnak, Enhanced photocatalytic activities of Bi_2WO_6/BiOCl

483 composite synthesized by one-step hydrothermal method with the assistance of HCl. Mater.
484 Sci. Semicond. Process **89**, 32–40 (2019) https://doi:10.1016/j.mssp.2018.08.026
485 [38] L. Hao, L. Kang, H. Huang, L. Ye, K. Han, S. Yang, H. Yu, M. Batmunkh, Y. Zhang, T. Ma,
486 Surface-halogenation-induced atomic-site activation and local charge separation for superb
487 CO_2 photoreduction. Adv. Mater. **31**, 1900546 (2019) https://doi:10.1002/adma.201900546
488 [39] Y. Shang, Y. Cui, R. Shi, P. Yang, Effect of acetic acid on morphology of Bi_2WO_6 with
489 enhanced photocatalytic activity. Mater. Sci. Semicond. Process **89**, 240–249 (2019)
490 https://doi:10.1016/j.mssp.2018.09.026
491 [40] M. Liang, Z. Yang, Y. Yang, Y. Mei, H. Zhou, S. Yang, One-step introduction of metallic Bi
492 and non-metallic C in Bi_2WO_6 with enhanced photocatalytic activity. J. Mater. Sci.: Mater.
493 Electron. **30**, 1310–1321 (2018) https://doi:10.1007/s10854-018-0400-7
494 [41] J. Gurgul, M.T. Rinke, I. Schellenberg, R. Pöttgen, The antimonide oxides REZnSbO and
495 REMnSbO (RE = Ce, Pr) - An XPS study. Solid State Sci. **17**, 122–127 (2013)
496 https://doi:10.1016/j.solidstatesciences.2012.11.014
497 [42] C. Zheng, H. Yang, Assembly of Ag_3PO_4 nanoparticles on rose flower-like Bi_2WO_6
498 hierarchical architectures for achieving high photocatalytic performance. J. Mater. Sci.: Mater.
499 Electron. **29**, 9291–9300 (2018) https://doi:10.1007/s10854-018-8959-6
500 [43] J. Di, C. Chen, C. Zhu, M. Ji, J. Xia, C. Yan, W. Hao, S. Li, H. Li, Z. Liu, Bismuth vacancy
501 mediated single unit cell Bi_2WO_6 nanosheets for boosting photocatalytic oxygen evolution.
502 Appl. Catal. B **238**, 119–125 (2018) https://doi:10.1016/j.apcatb.2018.06.066
503 [44] T. Wu, G. Liu, J. Zhao, H. Hidaka, N. Serpone, Photoassisted degradation of dye pollutants. V.
504 Self-photosensitized oxidative transformation of rhodamine B under visible light irradiation

505 in aqueous TiO_2 dispersions. J. Phys. Chem. B **102**, 5845–5851 (1998)
506 https://doi:10.1021/jp980922c
507 [45] J. Li, X. Yang, X. Yu, L. Xu, W. Kang, W. Yan, H. Gao, Z. Liu, Y. Guo, Rare earth
508 oxide-doped titania nanocomposites with enhanced photocatalytic activity towards the
509 degradation of partially hydrolysis polyacrylamide. Appl. Surf. Sci. **255**, 3731–3738 (2009)
510 https://doi:10.1016/j.apsusc.2008.10.029
511 [46] Z.M. El-Bahy, A.A. Ismail, R.M. Mohamed, Enhancement of titania by doping rare earth for
512 photodegradation of organic dye (Direct Blue). J. Hazard. Mater. **166**, 138–143 (2009)
513 https://doi:10.1016/j.jhazmat.2008.11.022
514 [47] P. Zhang, Y. Yi, C. Yu, W. Li, P. Liao, R. Tian, M. Zhou, Y. Zhou, B. Li, M. Fan, L. Dong,
515 High photocatalytic activity of lanthanum doped Bi_2MoO_6 nanosheets with exposed (0 0 1)
516 facets. J. Mater. Sci.: Mater. Electron. **29**, 8617–8629 (2018)
517 https://doi.org/10.1007/s10854-018-8876-8
518

519 **Figures Caption**

520 **Table 1** Comparison of photocatalytic performance of Pr-Bi_2WO_6 with previous reports.

521 **Figure 1a** X-ray diffraction patterns of the as-prepared samples.

522 **Figure 1b** X-ray diffraction patterns of the as-prepared samples (partial amplification drawings).

523 **Figure 2a** UV-Vis diffused reflection spectra of the as-prepared samples.

524 **Figure 2b** Band gap energy evaluation of the as-prepared samples.

525 **Figure 3** PL spectra of the undoped Bi_2WO_6 and 1% Pr-Bi_2WO_6 samples.

526 **Figure 4** XPS spectra of the undoped Bi_2WO_6 and 1% Pr-Bi_2WO_6 samples: (a) the survey spectra;

527 (b) Bi 4f spectra; (c) W 4f spectra; (d) O 1s spectra; (e) Pr 3d spectrum.

528 **Figure 5** SEM images of the undoped Bi_2WO_6 and 1% Pr-Bi_2WO_6 samples: (a and b), Bi_2WO_6; (c

529 and d), 1% Pr-Bi_2WO_6.

530 **Figure 6** (a and b) TEM and (c and d) HRTEM images of the 1% Pr-Bi_2WO_6 sample.

531 **Figure 7** N_2 gas adsorption-desorption isotherms (a and b) and the pore size distribution curves (c

532 and d) of the undoped Bi_2WO_6 and 1% Pr-Bi_2WO_6 samples.

533 **Figure 8** Adsorption of RhB in the presence of the as-prepared samples.

534 **Figure 9** Temporal evolution of the UV-Vis spectra for RhB catalyzed by 1% Pr-Bi_2WO_6 sample.

535 **Figure 10a** Degradation rates of RhB using Bi_2WO_6 catalysts doped with different amount of Pr.

536 **Figure 10b** Plots of $\ln(c_0/c)$ versus reaction time of the as-prepared samples.

537 **Figure 11** Recycling degradation curves of 1% Pr-Bi_2WO_6 sample for RhB.

538 **Figure 12** Effect of different scavengers on the degradation efficiency of RhB.

539 **Figure 13** Schematic diagram of the energy band levels of the 1% Pr-Bi_2WO_6 sample and the

540 proposed possible process for the photodegradation of RhB.

541

542 **Table 1.**

Dopant	Preparation method	Dye concentration	Degradation (%)	Time (min)	Ref.
La	hydrothermal	RhB (4 mg/L) / 100 mL	98	25	[26]
Eu	hydrothermal	RhB (10 mg/L) / 100 mL	90.2	60	[27]
Gd	microwave assisted	RhB	100	120	[28]
Lu	coprecipitation - thermal treatment	RhB (10^{-5} mol/L) / 200 mL	99.1	60	[29]
Sm	hydrothermal	RhB (20 mg/L) / 80 mL	100	40	[30]
Pr	hydrothermal	RhB (10^{-5} mol/L) / 100 mL	99.4	20	This work

543

544

545 **Fig. 1a.**

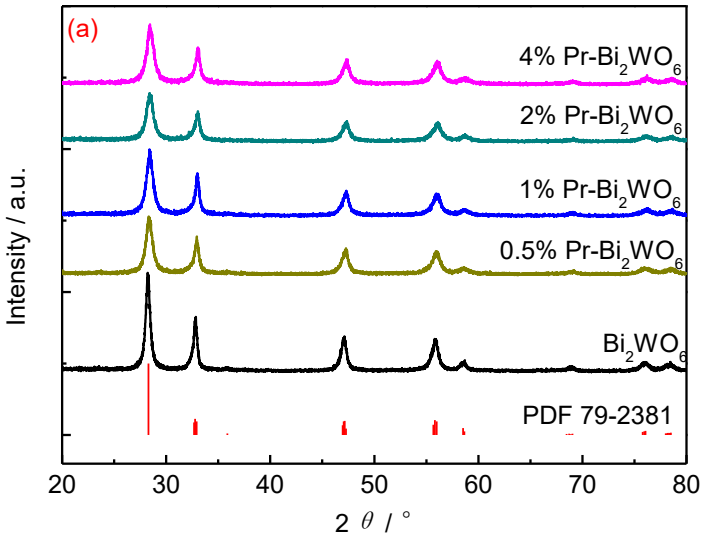

546

547

548 **Fig 1b.**

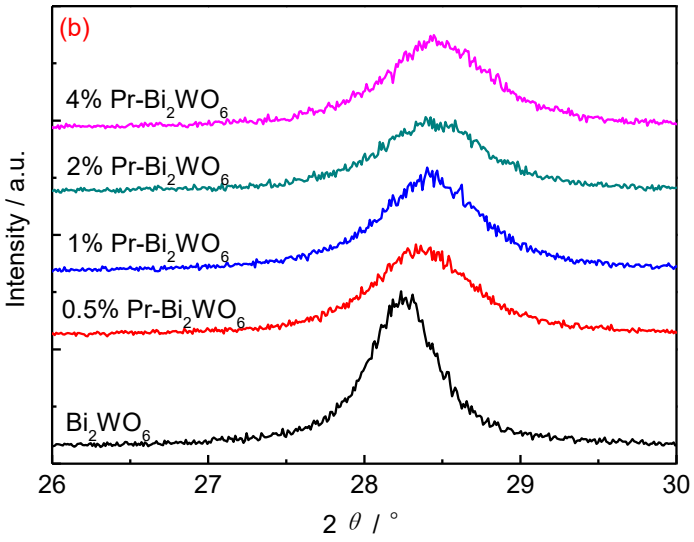

549

550

551 **Fig. 2a.**

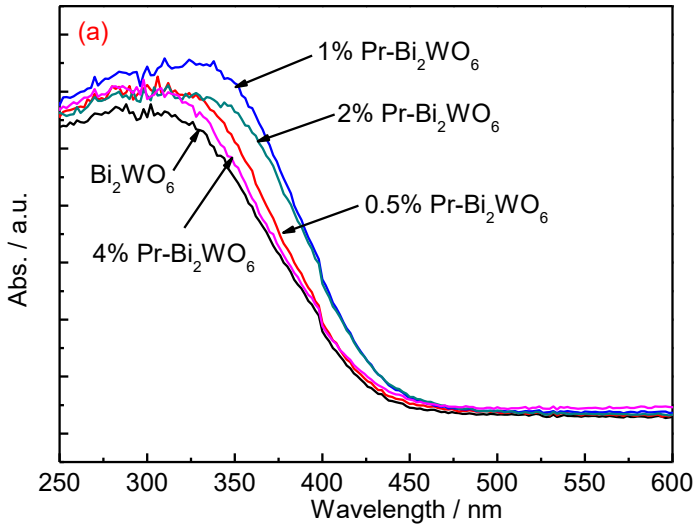

552

553

554 **Fig. 2b.**

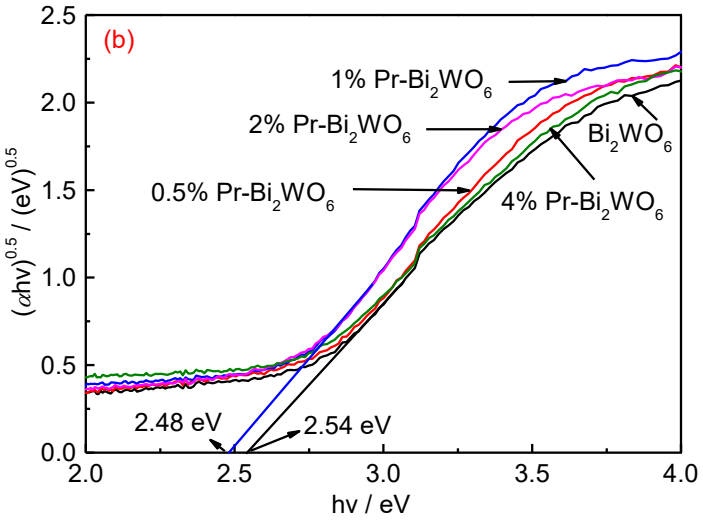

555

556

557 **Fig. 3.**

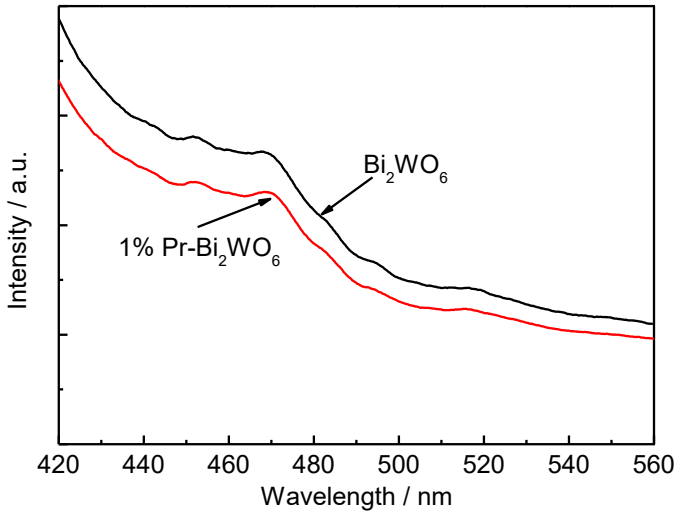

558

559

560 **Fig. 4a.**

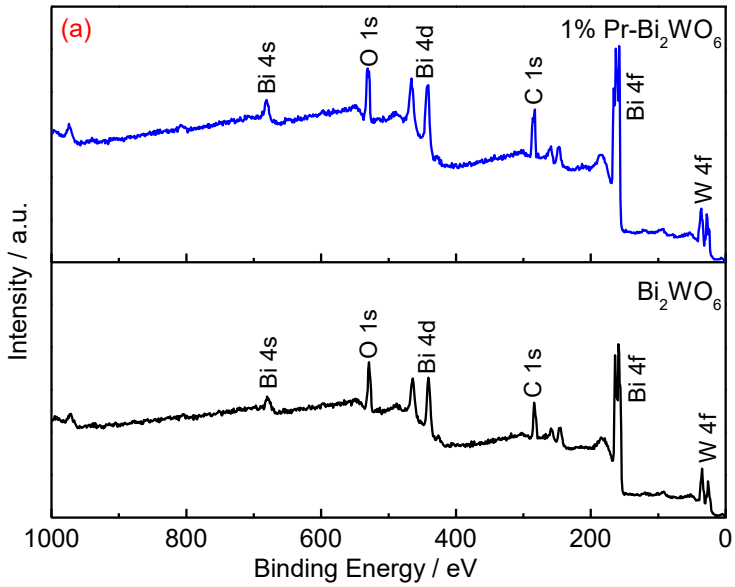

561
562

563 **Fig. 4b.**

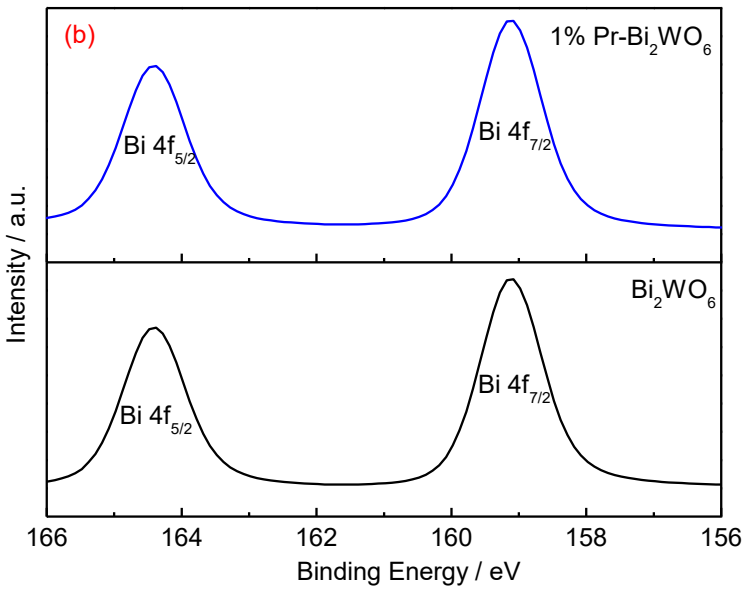

564

565

566 **Fig. 4c.**

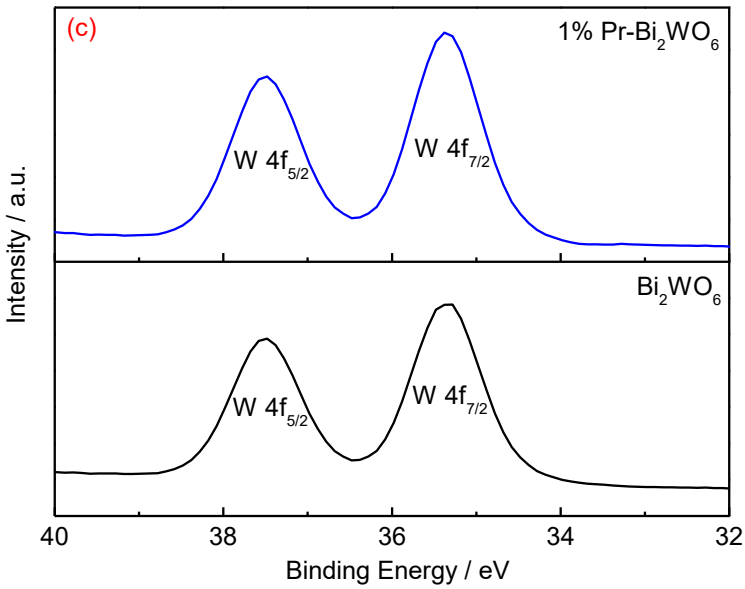

567

568

569 **Fig. 4d.**

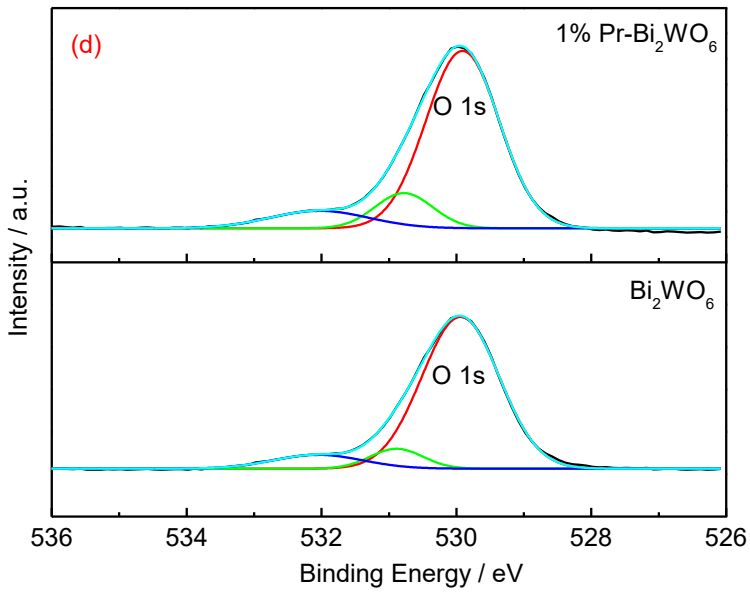

570

571

572 **Fig. 4e.**

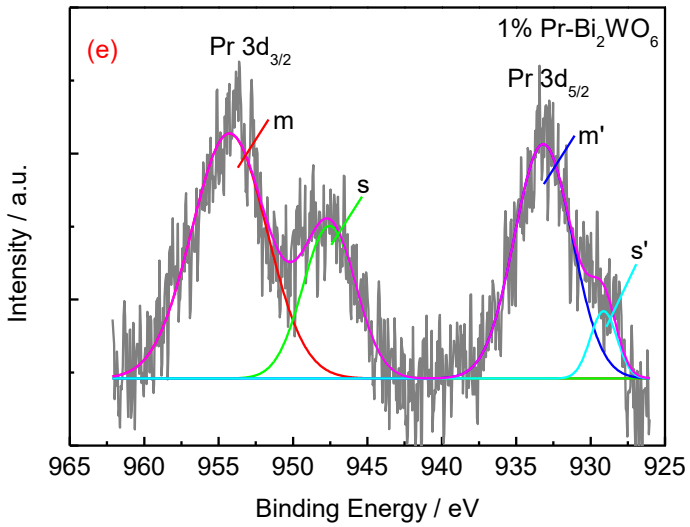

573

574

575 **Fig. 5.**

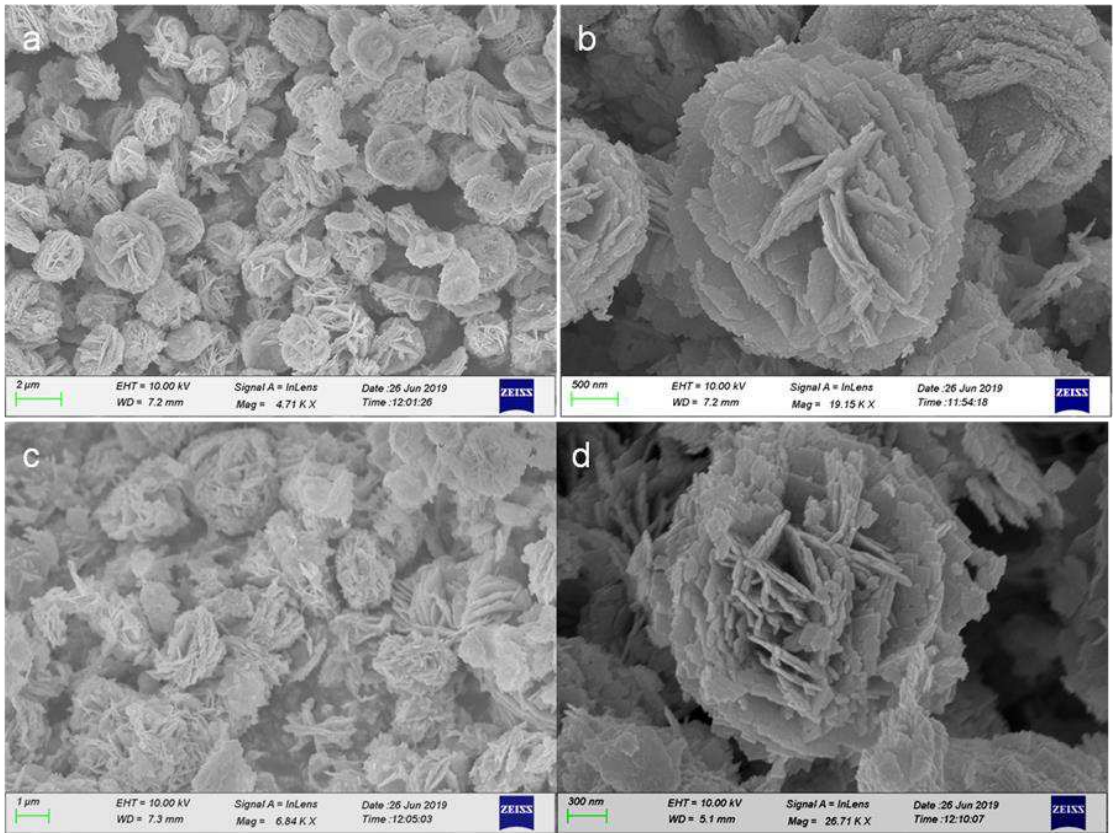

576

577

578 **Fig. 6.**

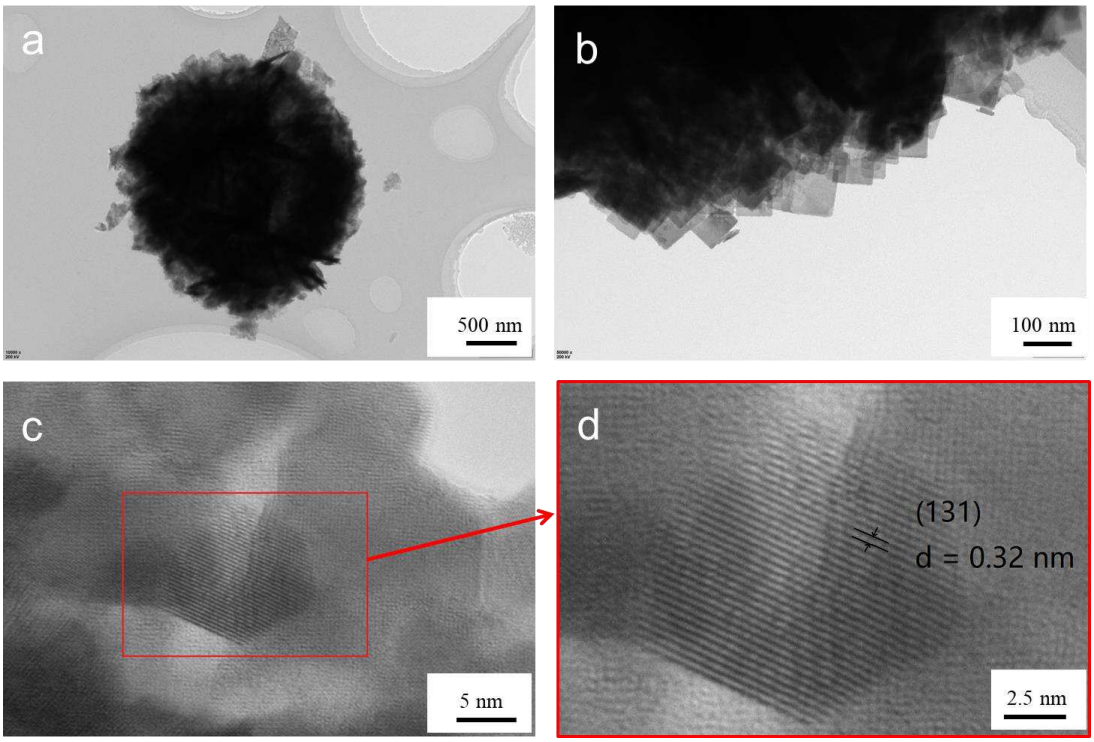

579

580

581 **Fig. 7.**

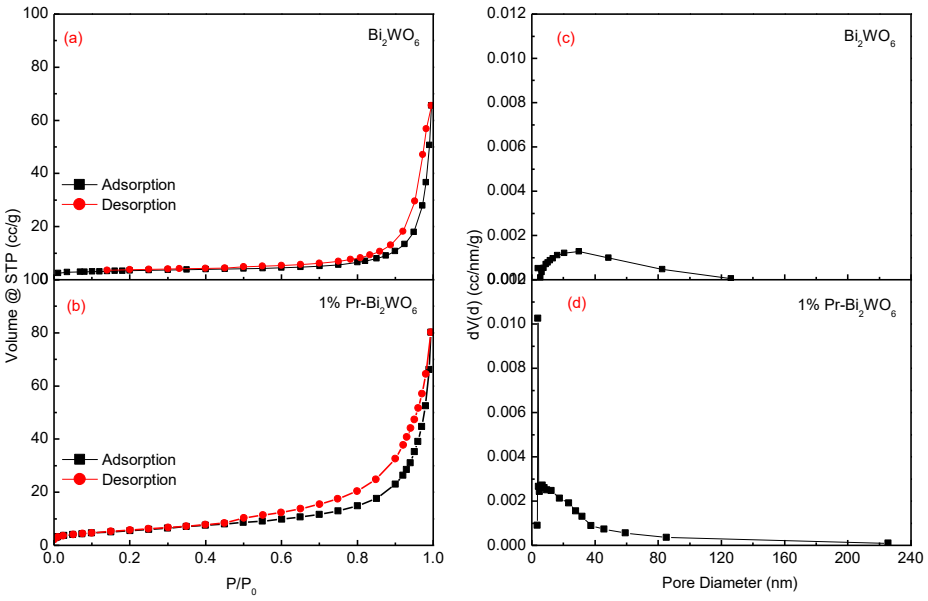

582

583

584 **Fig. 8.**

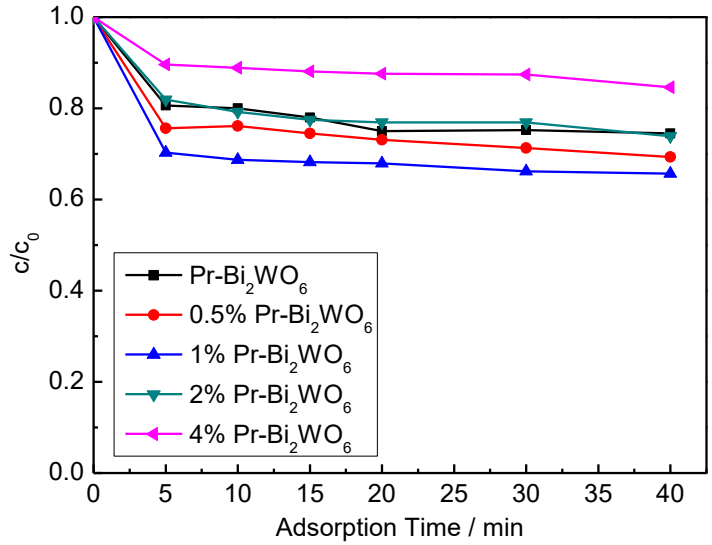

585

586

587 **Fig. 9.**

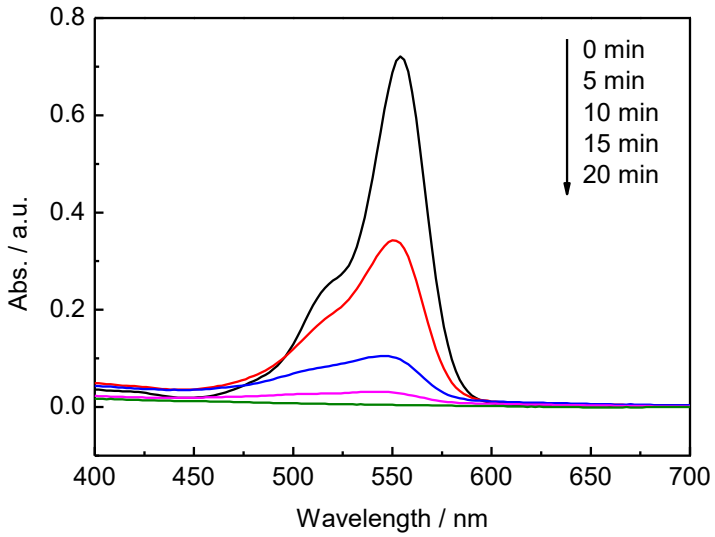

588

589

590 **Fig. 10a.**

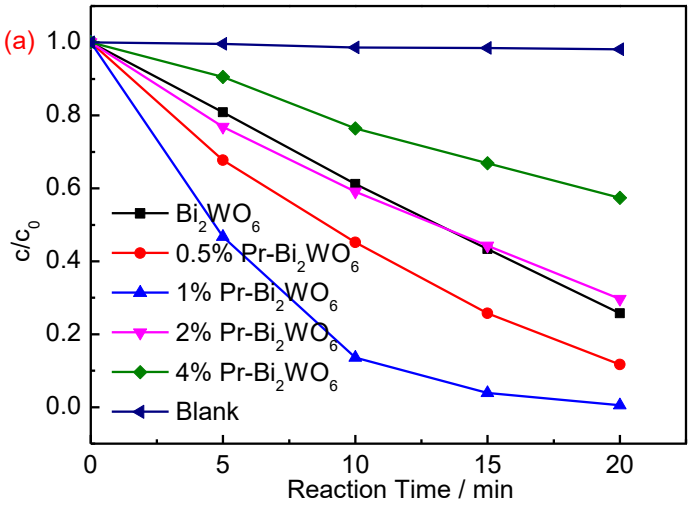

591

592

593 **Fig. 10b.**

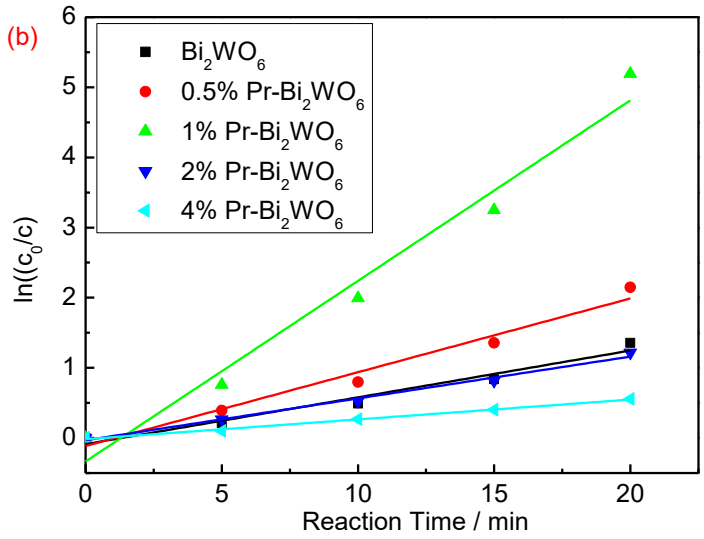

594

595

596 **Fig. 11.**

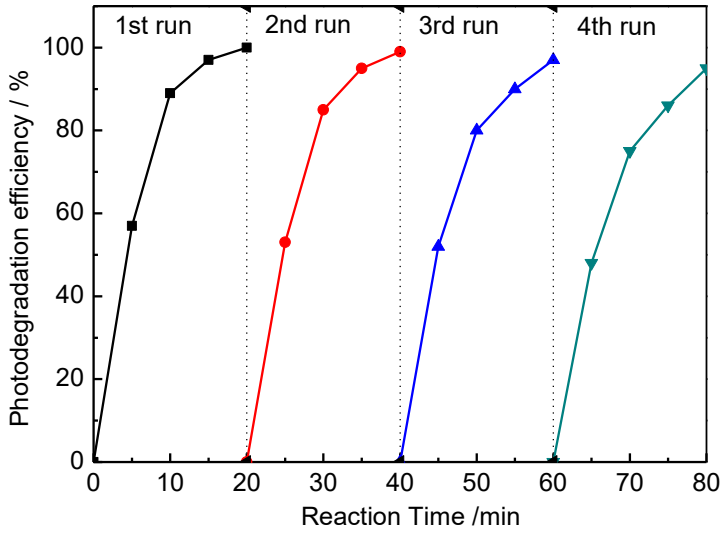

597

598

599 **Fig. 12.**

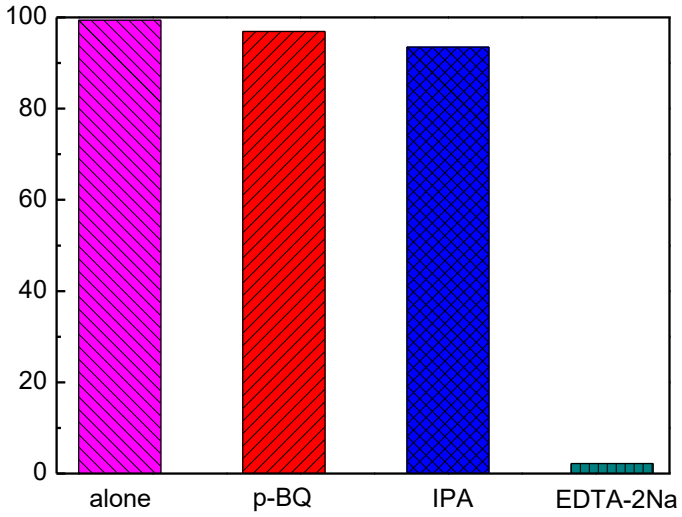

600

601

602 **Fig. 13.**

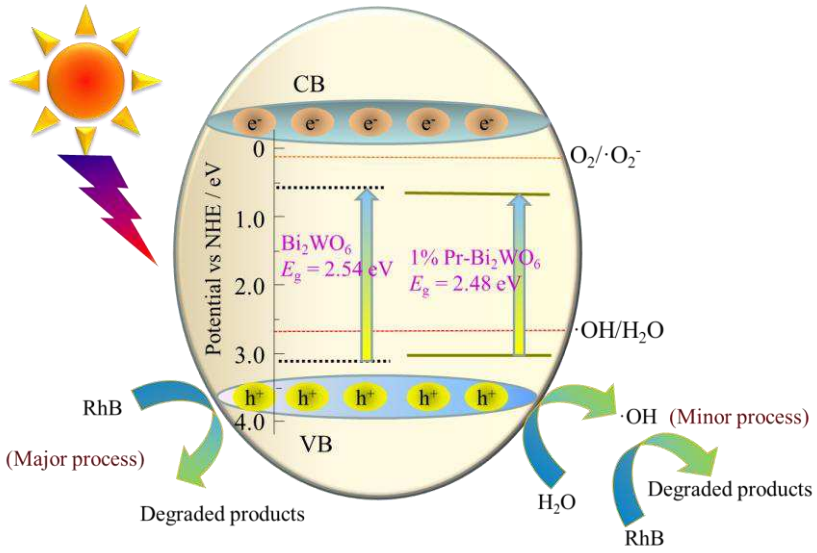

603